

Investigation of the effect of conjugate heat transfer on the adiabatic effectiveness of an annular gas turbine engine combustor

By M. Cui[†] AND S. Bose[‡]

Integrated analyses of major physical mechanisms associated with heat transfer are conducted for a realistic aircraft engine combustor. Coupled wall-modeled large-eddy simulations (WMLES) and conjugate heat transfer (CHT) analyses are performed to evaluate the unsteady turbulence structures on convective and conductive heat transfer inside the engine combustor. The impact of heat conduction through a solid liner material on overall heat transfer process is assessed by a comparative study of adiabatic and CHT cases. The results of integrated WMLES/CHT simulations agree with available test data. A non-dimensional parameter, liner cooling effectiveness, is introduced and validated to measure the effectiveness of the engine combustor cooling system.

1. Introduction

In a modern gas turbine engine (GTE) combustor, the gas temperature from the combustion process may reach 2400 K (Lefebvre & Ballal 2010). This temperature is significantly higher than the melting point of the combustor flame tube and other components. Therefore, cooling systems need to be developed to protect the combustor's structural integrity. As engines are designed to be more fuel efficient, the pressure ratio and temperature inside the combustors rises and the problem of wall cooling becomes more severe. Current combustor cooling technology often requires more than one-third of the total combustor airflow to be used to cool the combustor liner. One of the major challenges to improve the performance, reliability, and cost of aircraft engines is to develop more effective cooling technology.

As critical aspects of GTE combustor aerothermal design, the flows and heat transfer inside a GTE combustor need to be simulated in a realistic environment. Current aircraft engines use liquid aviation fuels, and these liquid fuels need to be atomized and vaporized before the combustion process starts. To initiate and sustain combustion, multiple sets of vanes and flow regulatory components are introduced to generate swirling turbulent flows for effective atomization and evaporation of the liquid jet fuel as well as recirculation of flames and hot gas. The resulting swirling velocity and temperature field distort the near-wall flow field and impact the integrity of air cooling films on the surface of the combustor liner (Mazzei *et al.* 2016). Combustor design and analysis must take these physical mechanisms (fuel atomization/evaporation, chemical reaction, flame and hot gas recirculation, and liner cooling flows) into account.

The combustor liner is a container for the flowing combustion hot gas and is surrounded by the combustor casing, with cool air flowing between the liner and the casing. The liner is heated mainly by hot gas and cooled by conduction through solid material and

[†] Naval Air Warfare Center Aircraft Division, Patuxent River

[‡] Cascade Technologies, Inc., Palo Alto

convection of air within the annulus. To assess the effectiveness of a cooling system, the heat transfer process needs to be analyzed by coupling a high-fidelity unsteady flow calculation with the heat conduction through the solid body (conjugate heat transfer).

This report summarizes an effort to apply an efficient strategy for tightly coupling conjugate heat transfer (CHT) effects with a wall-modeled large-eddy simulation (WMLES) approach in order to analyze CHT process and evaluate the combustor liner cooling effectiveness. The technology is demonstrated in an integrated fashion for a realistic GTE combustor and validated with available test data. The methodology developed and data obtained can be readily applied to GTE combustor cooling system design and analysis.

2. Formulation and computational setup

2.1. Filtered LES equations for gas phase

Large-eddy simulations (LES) of GTE combustion and heat transfer processes are conducted using the technique developed by Moin & Apte (2006). For completeness, the gas-phase continuity, scalar mixture fraction, progressive variable, and momentum equations are

$$\frac{\partial \bar{\rho}_g \tilde{\mathbf{u}}_j}{\partial x_j} = \frac{\partial \bar{\rho}_g}{\partial t} + \bar{S}_m, \quad (2.1)$$

$$\frac{\partial (\bar{\rho}_g \tilde{Z})}{\partial t} + \frac{\partial (\bar{\rho}_g \tilde{Z} \tilde{\mathbf{u}}_j)}{\partial x_j} = \frac{\partial}{\partial t} (\bar{\rho}_g \tilde{\alpha}_Z \frac{\partial \tilde{Z}}{\partial x_j}) + \frac{\partial \mathbf{q}_{Zj}}{\partial x_j} + \bar{S}_Z, \quad (2.2)$$

$$\frac{\partial (\bar{\rho}_g \tilde{C})}{\partial t} + \frac{\partial (\bar{\rho}_g \tilde{C} \tilde{\mathbf{u}}_j)}{\partial x_j} = \frac{\partial}{\partial t} (\bar{\rho}_g \tilde{\alpha}_C \frac{\partial \tilde{C}}{\partial x_j}) + \frac{\partial \mathbf{q}_{Cj}}{\partial x_j} + \bar{\omega}_C, \text{ and} \quad (2.3)$$

$$\frac{\partial (\bar{\rho}_g \tilde{\mathbf{u}}_{ij})}{\partial t} + \frac{\partial (\bar{\rho}_g \tilde{\mathbf{u}}_i \tilde{\mathbf{u}}_j)}{\partial x_j} = -\frac{\partial p}{\partial x_i} + \frac{\partial (2\mu \tilde{S}_{ij})}{\partial x_j} + \frac{\partial \mathbf{q}_{ij}}{\partial x_j} + \bar{S}_i, \quad (2.4)$$

where

$$S_{ij} = \frac{1}{2} \left(\frac{\partial \tilde{\mathbf{u}}_i}{\partial x_j} + \frac{\partial \tilde{\mathbf{u}}_j}{\partial x_i} \right) - \frac{1}{3} \delta_{ij} \frac{\partial \tilde{\mathbf{u}}_k}{\partial x_k}, \text{ and} \quad (2.5)$$

$$\bar{\omega}_C = \int \dot{\omega}_C(Z, C) \tilde{P}(Z, C) dZ dC. \quad (2.6)$$

In these equations, ρ_g is the gas phase density, u_j is the velocity vector, p is the pressure, μ is the dynamic viscosity, δ_{ij} is the Kronecker symbol, Z is the mixture fraction, C is the progress variable, α_Z and α_C are the scalar diffusivities, and $\dot{\omega}_C$ is the source term due to chemical reaction. The filter operation is denoted by an overbar and Favre (density-weighted) filtering by a tilde. The additional terms (\bar{S}_m , \bar{S}_Z , and \bar{S}_i) in the continuity, mixture-fraction, and momentum equations are the interphase mass and momentum transport terms. The unclosed transport terms in the momentum and scalar equations are grouped into the residual stress q_{ij} and scalar fluxes q_{Zj} and q_{Cj} . The joint subscale probability density function (PDF) is modeled by writing $\tilde{P}(Z, C) = \tilde{P}(Z|C)\tilde{P}(C)$. $\tilde{P}(Z)$ is modeled by the presumed beta subgrid PDF, and the conditional PDF $\tilde{P}(Z|C)$ is modeled as a delta function according to Pierce & Moin (2004).

The subgrid terms are closed using the dynamic Smagorinsky model (Moin *et al.* 1991).

The eddy viscosity, eddy diffusivities, and subfilter variance of the mixture fraction are evaluated as

$$\mu_t = \bar{\rho}_g C_\mu \Delta^2 |\tilde{\mathbf{S}}|, \quad (2.7)$$

$$\bar{\rho}_g \alpha_t = \bar{\rho}_g C_\alpha \Delta^2 |\tilde{\mathbf{S}}|, \text{ and} \quad (2.8)$$

$$\bar{\rho}_g \widetilde{Z''^2} = \bar{\rho}_g C_\alpha \Delta^2 |\nabla \tilde{\mathbf{Z}}|^2, \quad (2.9)$$

where $|\tilde{\mathbf{S}}| = \sqrt{\tilde{S}_{ij}\tilde{S}_{ij}}$, C_μ , C_α , and $C_{\bar{Z}}$ are evaluated dynamically (Pierce & Moin 1998).

2.2. Liquid-phase equations

If the density of the liquid fuel droplets is much larger than that of the air, the sizes of the liquid fuel droplets are small compared to the turbulence integral length scale, and the effect of the shear on the droplets' motion is negligible. The Lagrangian equations governing the motion of droplets can be expressed as (Crowe *et al.* 1998)

$$\frac{d\mathbf{x}_p}{dt} = \mathbf{u}_p \text{ and} \quad (2.10)$$

$$\frac{d\mathbf{u}_p}{dt} = D_{p_{drag}}(\mathbf{u}_g - \mathbf{u}_p) + \left(1 - \frac{\rho_g}{\rho_p}\right)\mathbf{g}, \quad (2.11)$$

where \mathbf{x}_p is the position of the droplet centroid, \mathbf{u}_p is the droplet velocity, \mathbf{u}_g is the gas velocities interpolated to the droplet location. ρ_g and ρ_p are the droplet and gas densities, and \mathbf{g} is gravitational acceleration. The drag on a droplet is modeled by the drag coefficient C_d as

$$D_{p_{solid}} = \frac{3}{4}C_d\left(\frac{\rho_g}{\rho_p}\right)(|\mathbf{u}_g - \mathbf{u}_p|/|\mathbf{d}_p|), \quad (2.12)$$

where C_d is obtained from the nonlinear correlation correction (Crowe *et al.* 1998)

$$C_d = 24/Re_p(1 + aRe_p^b), \quad (2.13)$$

where $a = 0.15$, $b = 0.687$, and $Re_p \leq 800$.

The ellipticity, E , is introduced to model droplet deformation as

$$E = 1 - 0.11We^{0.82} + 0.013\sqrt{\frac{\rho_p}{\rho_g}\left(\frac{\mu_g}{\mu_l}\right)}Oh^{0.55}We^{1.1}. \quad (2.14)$$

The nondimensional Weber and Ohnesorge numbers are defined as $We = \rho_g U^2 d_p \sigma$ and $Oh = \mu_l / \sqrt{\rho_p \sigma d_p}$, where U is the relative velocity between gas and liquid, d_p is the diameter of the droplet, and σ is the surface tension. The impact of droplet deformation on drag and drag coefficient is calculated through effective droplet diameter, $d_p^* = d_p E^{-1/3}$, and particle Reynold number, $Re_p^* = Re_p E^{-1/3}$.

The Lagrangian equation of particle mass and heat transfer processes are applied to liquid evaporation as

$$\frac{d\mathbf{m}_p}{dt} = -\dot{\mathbf{m}}_p \text{ and} \quad (2.15)$$

$$m_p C_{pl} \frac{dT_p}{dt} = h_p \pi d_p^2 (T_g - T_p) - \dot{m}_p \Delta h_v, \quad (2.16)$$

where Δh_v is the latent heat of vaporization, m_p is the mass of the droplet, T_p is the temperature of the droplet, and C_{pl} is the specific heat of liquid. The diameter of the droplet is linked to its mass, $d_p = (6m_p)/(\pi\rho_p)^{1/3}$. The effective heat transfer coefficient, h_p , is defined as

$$h_p = k_s \left(\frac{dT_p}{dr} \right)_{sg} / (T_g - T_s), \quad (2.17)$$

where k_s is the effective conductivity of the surrounding gas at the droplet surface. The subscript s stands for the surface of the droplet.

2.3. Interface exchange terms

The source terms in the gas continuity, mixture-fraction, and momentum equations are obtained from the equations governing droplet dynamics (Moin & Apte 2006). The interpolation from the particle position, \mathbf{x}_p , to the centroid of the grid control volume is conducted using an interpolation operator. The expressions for source terms are

$$\bar{S}_m = \bar{S}_Z = - \sum_k \mathcal{G}_\sigma(\mathbf{x}, \mathbf{x}_p) \frac{d}{dt}(\mathbf{m}_p) \quad \text{and} \quad (2.18)$$

$$\bar{S}_i = - \sum_k \mathcal{G}_\sigma(\mathbf{x}, \mathbf{x}_p) \frac{d}{dt}(\mathbf{m}_p) \mathbf{u}_{pi}^k, \quad (2.19)$$

where summation is over all droplets (k) and the function \mathcal{G}_σ is the interpolation operator

$$\mathcal{G}_\sigma(\mathbf{x}, \mathbf{x}_p) = \frac{1}{(\sigma\sqrt{2\pi})^3} \exp\left[-\frac{\sum_{i=1}^3 (\mathbf{x}_i - \mathbf{x}_{pi})^2}{2\sigma^2}\right], \quad (2.20)$$

where σ is proportional to the grid size in which the droplet lies. For each droplet, the conservation constraint

$$\int_{V_{cv}} \mathcal{G}_\sigma(\mathbf{x}, \mathbf{x}_p) dV = 1 \quad (2.21)$$

is imposed by normalizing the interpolation operator. V_{cv} is the volume of the grid cell in which the droplet lies.

2.4. Wall models for turbulent heat fluxes in LES

CHT analyses require fine near-wall grids to resolve flow and heat transfer physics through boundary layers to viscous sublayer and adjacent solid surfaces. Since the Reynolds number is high in GTE combustors, it becomes prohibitively expensive to use LES to resolve the relevant viscous sublayer ($l_\nu = \nu/u_\tau$, where ν is the kinetic viscosity and u_τ is the wall friction velocity). To improve the LES efficiency of CHT predictions in GTE combustors, the heat flux at the solid wall is modeled (Bose & Park 1990). The wall models used in CHT analyses assume the absence of pressure gradient and unsteadiness and make equilibrium approximations about the boundary layer on the solid surfaces as

$$\frac{d}{dy}((\mu + \mu_t) \frac{du}{dy}) = 0, \mu_t = \kappa y \mu_\tau D(y^+), \tau_w = \mu \frac{du}{dy}|_w, \quad (2.22)$$

subject to

$$u(y = 0) = 0, u(y_1) = u_{LES}, \quad (2.23)$$

where μ and μ_t denote the dynamic viscosity and turbulent eddy viscosity, respectively; u denotes the locally streamwise velocity; κ is the von Karman constant; τ_w is the wall stress; and y denotes the locally wall normal direction. These equations are coupled to boundary conditions: no-slip at the wall and continuity with the LES velocity field at some distance in the interior.

The turbulent heat flux is modeled under similar approximations as

$$\frac{d}{dy}((\mu + \mu_t)u \frac{du}{dy} + (k + k_t) \frac{dT}{dy}) = 0, k_t = \frac{\mu_t c_p}{Pr_t}, q_w = k \frac{dT}{dy}|_w, \quad (2.24)$$

subject to

$$T(y = 0) = 0, T(y_1) = T_{LES}, \quad (2.25)$$

where k and k_t denote the thermal conductivity and the turbulent thermal conductivity, respectively; T is the temperature; Pr_t is the turbulent Prandtl number; and q_w is the wall heat flux. Similarly, these equations are coupled to thermal boundary conditions at the wall and to the interior LES thermal field.

2.5. Time integration strategies for LES with CHT

For GTE thermal system development, it usually take significant time for engines to reach thermal equilibrium. Therefore, there is a need to efficiently integrate the disparate time scales between the near-wall turbulent eddies (that are the leading order transport mechanism of heat/enthalpy to the wall) and heat conduction in the solid structure. Allowing the solid metal components to heat to near equilibrium temperature would potentially require integrating flow solutions for thousands of flow-through times, rendering a high-fidelity LES with CHT infeasible. The approach adapted in the present LES/CHT effort accelerates the thermal soaking of the material while maintaining a constant Biot number. The unsteady heat conduction equation governing the temperature of the solid components and its corresponding boundary conditions are

$$\frac{\partial(\rho C_p T)}{\partial t} + \frac{\partial}{\partial x_j} (k \frac{\partial T}{\partial x_j}) = 0, \quad (2.26)$$

subject to

$$k \frac{\partial T}{\partial n} = q_{w,LES}, \quad (2.27)$$

where ρ denotes the solid density, C_p is the heat capacity, T is the solid temperature, k denotes the thermal conductivity, and q_w is the wall heat flux (obtained from the fluid LES). As the system reaches a quasi-stationary state (the metal temperatures change slowly with respect to the fluid timescales), the solid temperature boundary conditions can be written in a non-dimensional form as

$$\frac{\partial(T/\Delta T)}{\partial(n/L)} = \frac{q_w L}{k \Delta T} = \left(\frac{hL}{k}\right) = Bi, \quad (2.28)$$

where ΔT denotes a relevant temperature change, L is a characteristic length scale of the body, h is a heat transfer coefficient, and Bi denotes the Biot number. In order to prevent the quasi-steady solution from being artificially contaminated, the physical Biot

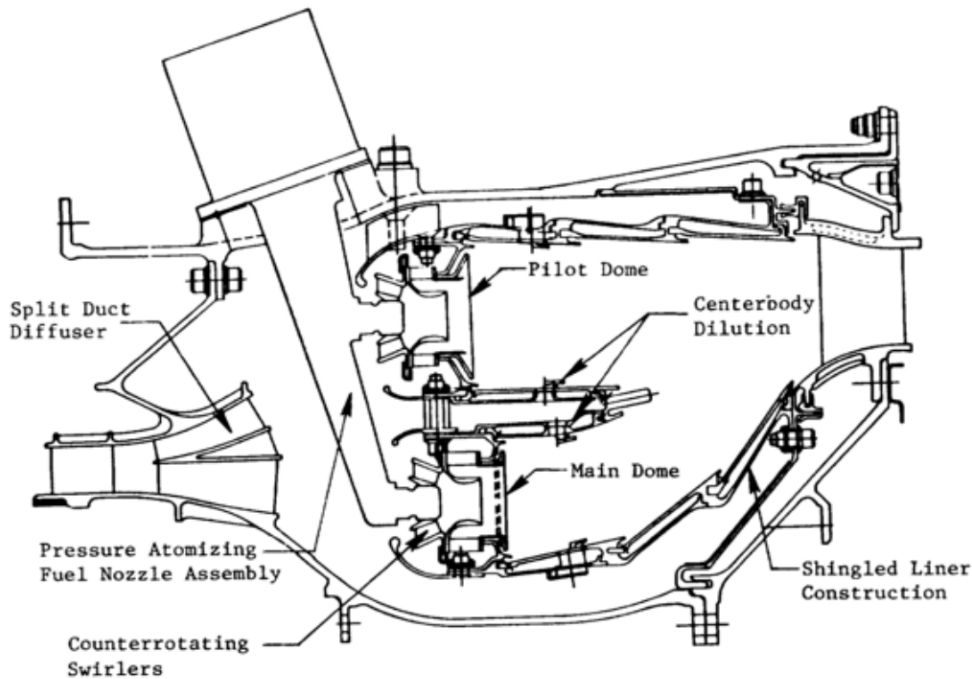


FIGURE 1. A cross section of EEE combustor.

number is maintained. This condition leads to the constraint that wall heat flux, thermal conductivity, and solid geometry be kept constant during thermal soaking.

2.6. NASA EEE combustor

The NASA energy efficient engine (EEE) combustor is the chosen combustor for our investigation. The EEE combustor is a realistic annular GTE combustor, for which, the full design and geometry can be found in publicly available literature. A cross section of the NASA EEE combustor is shown in Figure 1. Previous work by Burrus *et al.* (1984) produced detailed EEE geometric and operational information as well as data from experimental measurements performed on the GTE combustor. The current work reports the integrated WMLES/CHT simulations on the entire EEE combustor. These simulations include the modeling of all relevant geometry (combustor casing, liner, diffuser, and fuel injectors). The combustor liner cooling system includes film-cooling and effusion-cooling holes in the shingled combustor liner.

3. Results and discussion

3.1. Methodology of the investigation

To isolate the effects of upstream and downstream components and physical mechanisms that are not included in our current effort, the investigation is conducted comparatively. The first set of WMLES for the EEE combustor is conducted with the assumption that all walls in the EEE combustor are adiabatic. The second set is conducted with the assumption that the solid walls of the combustor's inner and outer liners are conductive while other walls of the combustor are adiabatic. The differences in the temperature

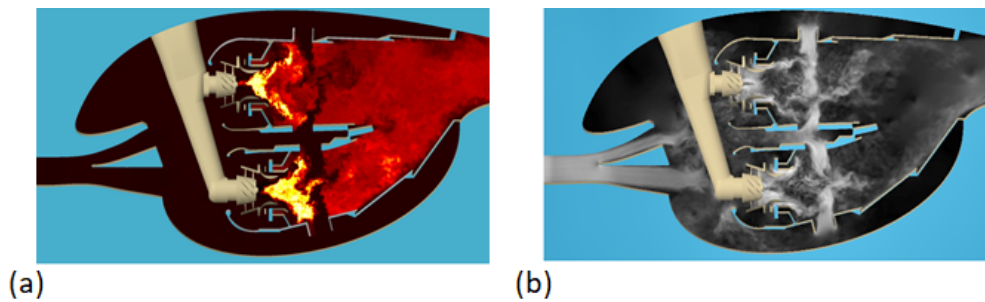


FIGURE 2. The instantaneous distributions of (a) temperature and (b) velocity.

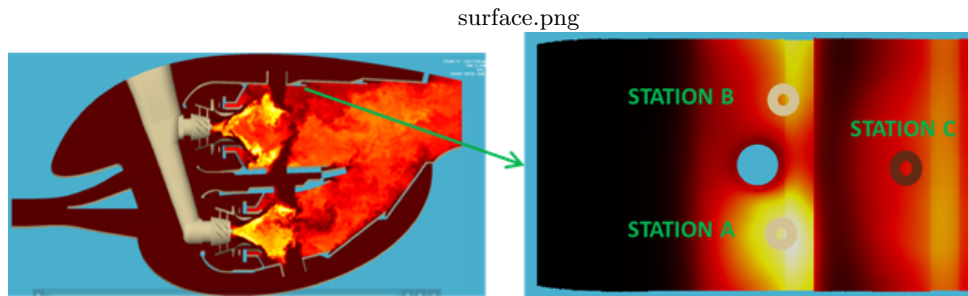


FIGURE 3. Temperature distribution on the surface of the combustor liner.

distributions are calculated to reveal the impact of the CHT process. Figure 2 shows the representative instantaneous temperature and velocity distributions. WMLES predictions are performed continuously until the mean field variables are stable. Both mean and instantaneous values of the field variables are recorded for post processing.

3.2. Validation of WMLES models and results

To ensure that the integrated models and obtained results are capturing the dominant physical mechanisms, a validation study was performed for the WMLES of the EEE combustor. The combustor inlet pressure and temperature for the case chosen are 12.2 bar and 640 K, respectively. The aviation fuel used in the case is a Jet-A surrogate, and the fuel/air ratio is 0.0143. The material for the combustor's inner and out liners is an uncoated X-40 alloy. The values of the liner metal wall temperature at the three stations (A, B, and C), where the temperature measurements were taken (Burrus *et al.* 1984), are calculated. The Figure 3 shows the relative positions of the three stations inside the EEE combustor. The results of the adiabatic WMLES analyses, the integrated WMLES/CHT analyses, and the temperature measurements are shown in Figure 4. The values listed are the relative temperature respect to the combustor inlet. The liner wall temperature values at the three stations for the CHT case show good agreement against the Burrus *et al.* (1984) measurements. The adiabatic temperature values at the liner walls are higher than the values for the CHT case and measurements. It reflects a directional correct results because the thermal energy transport through the solid liner materials in the CHT case should reduce the liner wall temperature.

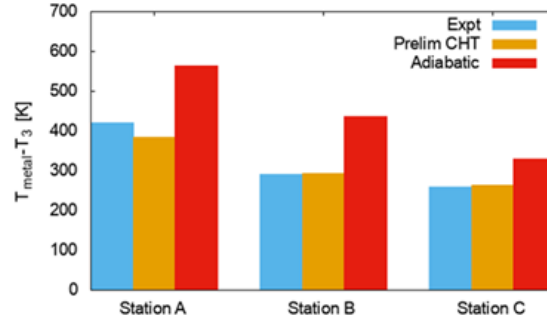


FIGURE 4. Comparisons with the measurements in Burrus et al. (1984).

	$T_3, ^\circ K$	P_3, bar	F/A
simulation 1	720	2.5	0.0140
simulation 2	640	12.2	0.0143

TABLE 1. Operating conditions for simulation 1 and simulation 2.

3.3. Liner cooling effectiveness

The results of WMLES for the EEE combustor flow and heat transfer are time series of pressure, temperature and velocity values for both liquid and gas phases. The ranges of these instantaneous values also change significantly at different GTE operating conditions. To generalize the simulation results and provide the guidance for the combustor designers to design and optimize the combustor cooling systems for different engines at various operating conditions, a non-dimensional quality, liner cooling effectiveness, η , is introduced.

The non-dimensional liner cooling effectiveness is defined as

$$\eta = \frac{T_{out,h} - T_{cht,w}}{T_{out,h} - T_{in,c}}, \quad (3.1)$$

where η is the liner cooling effectiveness, $T_{out,h}$ is the combustor outlet temperature, $T_{in,c}$ is the combustor inlet temperature, and $T_{cht,w}$ is the combustor liner surface temperature. Two integrated WMLES/CHT simulations with different inlet pressures and temperatures were conducted to evaluate the applicability of the liner cooling effectiveness in the GTE combustor. The objective of the simulations is to examine if the liner cooling effectiveness can characterize the cooling system performance at representative GTE operating conditions. The operating conditions for both cases are listed in Table 1, where T_3 is the combustor inlet temperature, P_3 is the combustor inlet pressure, and F/A is the fuel/air ratio.

The critical physical features of the EEE combustor flow and heat transfer can be observed in the liner cooling effectiveness plots in Figure 5. When the film cooling sheets

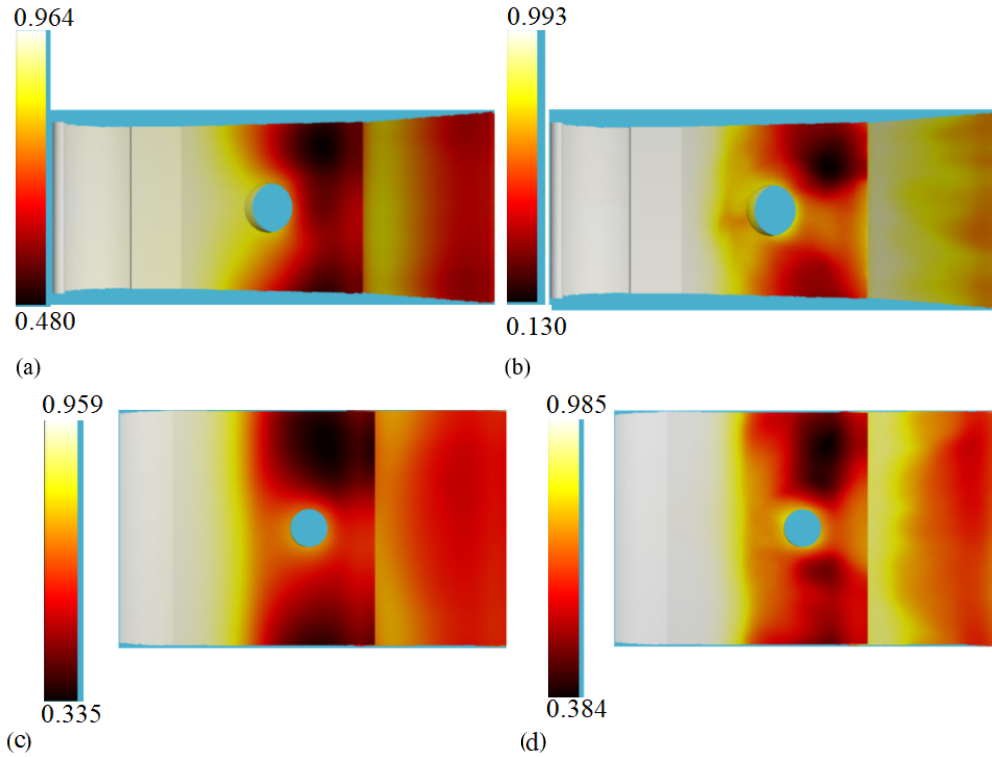


FIGURE 5. Liner cooling effectiveness on EEE combustor for (a) inner liner case 1, (b) inner liner case 2, (c) outer liner case 1, and (d) outer liner case 2.

come out from the injection gap, the liner cooling effectiveness is high. As the film cooling sheets are gradually broken by growing turbulence boundary layers, the cooling effectiveness decreases. The vortex formed around the dilution air jets can be seen on both sides of the dilution holes. The asymmetric flow field induced by air swirling elements around the dilution holes also can be identified.

4. Conclusions

Integrated CHT analyses of a realistic GTE combustor using WMLES were performed. The simulated physical mechanisms and their interactions are consistent with experimental observations. Quantitative comparisons of the coupled WMLES and CHT simulations and the experimental measurement data show good agreement. A comparative study of the CHT and adiabatic cases demonstrates that the accuracy of the temperature prediction is greatly improved on the combustor liner walls. The non-dimensional parameter, liner cooling effectiveness introduced here, can be applied to general engine aerothermal design and analysis.

Acknowledgments

The authors are grateful for reviews and stimulating discussions provided by the combustion group of Center for Turbulence Research Summer Program 2022 led by Professors Kazuki Maeda, Thierry Poinso, and Jonathan Wang at Stanford University. The WMLES and CHT analyses in this report were conducted using CharLES, a solver developed

by Cascade Technologies, Inc. The help provided by Professor Parviz Moin, Dr. Frank Ham, and Dr. Lee Shunn is highly appreciated.

REFERENCES

- BOSE, S. T. & PARK, G. I. 2018 Wall-modeled large-eddy simulation for complex turbulent flows. *Annu. Rev. Fluid Mech.* **50**, 535–561.
- BURRUS, D. L., C’HAHROUR, C. A., FOLTZ, H. L., SABIA, P. E., SETO, S. P., & TAYLOR, J. R. 1984 Energy efficient engine: combustor test hardware: detailed design report. NASA/CR-1984-168301.
- CROWE, C., SOMMERFELD, M., & TSUJI, Y. 1998 *Multiphase Flows with Droplets and Particles*. CRC Press.
- LEFEBVRE, A. H. & BALLAL, D. R. 2010 *Gas Turbine Combustion Alternative Fuels and Emissions*. CRC Press.
- MAZZEI, M., ANDREINI, A., FACCHINI, B. & TURRINI, F. 2016 Impact of swirl flow on combustor liner heat transfer and cooling: a numerical investigation with hybrid Reynolds-averaged Navier-Stokes large eddy simulation models. *J. Eng. Gas Turb. Power* **138**, 051504.
- MOIN, P. & APTE, S. V. 2006 Large-eddy simulation of realistic gas turbine combustors. *AIAA J.* **44**, 698–708.
- MOIN, P., SQUIRES, K., CABOT, W. & LEE, S. 1991 A dynamic subgrid model for compressible turbulence and scalar transport. *Phys. of Fluids A* **3**, 2746–2757.
- PIERCE, C. D., & MOIN, P. 1998 A dynamic model for subgrid-scale variance and dissipation rate of a conserved scalar. *Phys. Fluids A* **10**, 3041–3044.
- PIERCE, C. D., & MOIN, P. 2004 Progress-variable approach for large-eddy simulation of turbulence non-premixed combustion. *J. Fluid Mech.* **504**, 73–94.